Optics Letters

Differential phase contrast intensity diffraction tomography

Zhidong Bai,[1,2,3,†] Shun Zhou,[1,2,3,†] Habib Ullah,[1,2,3] Linpeng Lu,[1,2,3] Qian Chen,[3,4] and Chao Zuo[1,2,3,*]

[1]Smart Computational Imaging Laboratory (SCILab), School of Electronic and Optical Engineering, Nanjing University of Science and Technology, Nanjing, Jiangsu Province 210094, China
[2]Smart Computational Imaging Research Institute (SCIRI) of Nanjing University of Science and Technology, Nanjing, Jiangsu Province 210019, China
[3]Jiangsu Key Laboratory of Spectral Imaging & Intelligent Sense, Nanjing, Jiangsu Province 210094, China
[4]chenqian@njust.edu.cn
[†]These authors contributed equally to this work.
[*]zuochao@njust.edu.cn

Received 4 June 2024; revised 24 October 2024; accepted 30 October 2024; posted 1 November 2024; published 27 November 2024

Intensity diffraction tomography (IDT) is a label-free computational microscopy technique that infers 3D refractive index (RI) and absorption distributions of objects from intensity-only measurements. Nevertheless, the inherent coherent image formation model requires sequential intensity measurements under various plane wave illuminations, resulting in time-consuming data acquisition and low imaging speed. In this Letter, we propose differential phase contrast intensity diffraction tomography (DPC-IDT), which leverages partially coherent illumination to extend the accessible spectrum range, thereby achieving high-speed, motion-free 3D tomographic microscopy. DPC-IDT integrates DPC illumination within the IDT framework, allowing 3D RI tomogram reconstruction from only four intensity images under matched asymmetric annular illumination. The effectiveness of DPC-IDT is experimentally validated by RI measurements of standard microspheres. We also demonstrate dynamic 3D imaging results of living PLC cells at a 25 Hz volume rate, highlighting its potential for high-speed biological imaging of unstained samples.

https://doi.org/10.1364/OL.531869

Optical diffraction tomography (ODT), originally proposed by Wolf in 1969, has emerged as an increasingly popular label-free microscopic technique facilitating the three-dimensional (3D) visualization of transparent samples through the reconstruction of volumetric refractive index (RI) distributions [1]. Traditional ODT combines optical holography with computed tomography, utilizing holographic interference to obtain the phase distribution of samples from various angles and performing synthetic aperture to invert the 3D RI distribution [2–4]. Unfortunately, these methods encounter intrinsic interferometric issues, including speckle noise and parasitic interference due to temporal coherence, impeding high-quality imaging. Additionally, the complex interferometric setups are incompatible with commercial microscopes, thereby restricting their widespread application in the biomedical field.

To fundamentally overcome these limitations, non-interferometric ODT aims to recover the RI distribution of samples from intensity-only measurements. This approach has garnered increasing attention due to its speckle-free imaging quality and compatibility with existing microscopes. In recent years, various types of non-interferometric ODT techniques have been developed vigorously. These methods utilize the scattered field information generated by illumination angle scanning or z-axial scanning samples to retrieve the 3D RI tomograms [5–8]. Intensity diffraction tomography (IDT) [9], a simple but effective non-interferometric ODT technique, enables the direct inversion of 3D RI and absorption from multiple 2D intensity at various angles by using a slice-wise deconvolution under the slice-based linear framework. However, the inherent coherent imaging model and inversion algorithm of IDT necessitate sequential detection of scattered fields under various plane wave illuminations, resulting in time-consuming data acquisition and low imaging speed. Multiplexed IDT and annular IDT [10,11] have been proposed to enhance acquisition rates and reduce dataset size, but these techniques essentially represent simple image multiplexing and sparse sampling in the frequency domain, rather than an elegant optical system modulation and transfer function optimization process. On the other hand, imaging a sample under partial coherent illumination allows for an expanded frequency range accessible to the objective lens, facilitating parallel detection of the object's spectral information [12–15]. Especially the utilization of differential phase contrast (DPC) illumination enables the transmission of whole phase information to the intensity, thereby yielding robust phase contrast on the in-focus detection plane [16,17]. Matched asymmetric annular DPC illumination further improves the imaging resolution to near the incoherent diffraction limit while boosting the low-frequency response of the phase transfer function

(PTF), breaking the trade-off between imaging resolution and contrast [18].

To achieve a faster imaging rate and reduce data burden, this Letter introduces a high-speed, motion-free tomographic imaging technique, termed differential phase contrast intensity diffraction tomography (DPC-IDT), which seamlessly integrates traditional IDT with the DPC illumination scheme within the derived partially coherent IDT framework. This approach allows retrieving 3D RI tomograms from only four intensity images captured under matched asymmetric annular DPC illumination by employing a partially coherent slice-wise deconvolution algorithm. In previous works, IDT models sample as a series of 2D slices in an axial direction, where the total scattered field of light passing through the sample is considered the coherent superposition of the scattered fields from each slice. The linear relationship between the permittivity contrast $\Delta\varepsilon$ and the recorded intensity in the in-focus plane under plane wave illumination in the frequency domain can be expressed as follows:

$$\tilde{I}_c(\mathbf{u},0\mid\mathbf{u}_{\text{in}}) = \tilde{I}_0^c + \int H_P^c(\mathbf{u},z\mid\mathbf{u}_{\text{in}})\,\widetilde{\Delta\varepsilon}_{re}(\mathbf{u},z) + H_A^c(\mathbf{u},z\mid\mathbf{u}_{\text{in}})\,\widetilde{\Delta\varepsilon}_{im}(\mathbf{u},z)dz, \tag{1}$$

where $\mathbf{u}$ denotes the transverse spatial frequency vector and $\mathbf{u}_{\text{in}}$ is the wave vector of the incident plane wave. H_P^c and H_A^c are the phase and absorption transfer functions in the coherent case for each slice at depth z, respectively. $\tilde{I}_0^c = S(\mathbf{u}_{\text{in}})\,|P(-\mathbf{u}_{\text{in}})|^2\,\delta(\mathbf{u})$ is the constant background intensity. $\widetilde{\Delta\varepsilon}_{re}$ and $\widetilde{\Delta\varepsilon}_{im}$ are the real and imaginary permittivity contrast spectra, corresponding to the RI and absorption parts of the sample, respectively. Considering that the measurement intensity conforms to the principle of incoherent superposition, we derive the partially coherent IDT forward model:

$$\tilde{I}_{pc}(\mathbf{u},0) = \tilde{I}_0^{pc} + \int H_P^{pc}(\mathbf{u},z\mid\mathbf{u}_{\text{in}})\,\widetilde{\Delta\varepsilon}_{re}(\mathbf{u},z) + H_A^{pc}(\mathbf{u},z\mid\mathbf{u}_{\text{in}})\,\widetilde{\Delta\varepsilon}_{im}(\mathbf{u},z)dz, \tag{2}$$

where $\tilde{I}_{pc}(\mathbf{u},0)$ is the recorded intensity in the in-focus plane under partially coherent illumination, while $\tilde{I}_0^{pc} = \iint S(\mathbf{u}_{\text{in}})\,|P(-\mathbf{u}_{\text{in}})|^2\,d^2\mathbf{u}_{\text{in}}\,\delta(\mathbf{u})$ is the background intensity. H_P^{pc} and H_A^{pc} are the partially coherent phase optical transfer function (POTF) and absorption optical transfer function (AOPT), respectively, expressing as follows:

$$H_P^{pc}(\mathbf{u},z) = \frac{i\Delta z k_0^2}{2}\iint P(\mathbf{u}-\mathbf{u}_{\text{in}})\,\frac{\exp\{-i[\eta(\mathbf{u}-\mathbf{u}_{\text{in}})-\eta(\mathbf{u}_{\text{in}})]z\}}{\eta(\mathbf{u}-\mathbf{u}_{\text{in}})} - P(\mathbf{u}+\mathbf{u}_{\text{in}})\,\frac{\exp\{i[\eta(\mathbf{u}+\mathbf{u}_{\text{in}})-\eta(\mathbf{u}_{\text{in}})]z\}}{\eta(\mathbf{u}+\mathbf{u}_{\text{in}})}d^2\mathbf{u}_{\text{in}}, \tag{3a}$$

$$H_A^{pc}(\mathbf{u},z) = -\frac{\Delta z k_0^2}{2}\iint P(\mathbf{u}-\mathbf{u}_{\text{in}})\,\frac{\exp\{-i[\eta(\mathbf{u}-\mathbf{u}_{\text{in}})-\eta(\mathbf{u}_{\text{in}})]z\}}{\eta(\mathbf{u}-\mathbf{u}_{\text{in}})} + P(\mathbf{u}+\mathbf{u}_{\text{in}})\,\frac{\exp\{i[\eta(\mathbf{u}+\mathbf{u}_{\text{in}})-\eta(\mathbf{u}_{\text{in}})]z\}}{\eta(\mathbf{u}+\mathbf{u}_{\text{in}})}d^2\mathbf{u}_{\text{in}}, \tag{3b}$$

where Δz is the axial sampling spacing and k_0 is the wavenumber. P denotes the objective pupil function and $\eta(\mathbf{u}) = \sqrt{k_0^2 - |\mathbf{u}|^2}$ is the axial wave vector. Equation (2) is applicable to arbitrary partial coherent illumination, and when discrete light-emitting diode (LED) illumination is used, the integral symbols in Eqs. (3a) and (3b) degenerate to discrete summation.

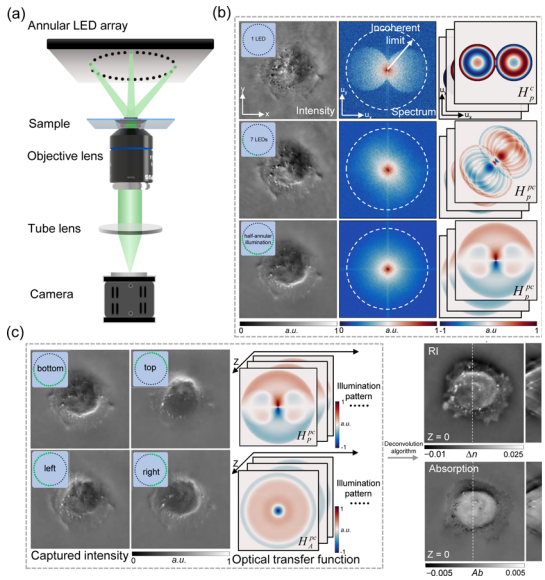

Fig. 1. Schematic diagram of the DPC-IDT imaging system and method. (a) Schematic diagram of the experimental setup and the illumination strategy. (b) Distributions of the captured intensity images, Fourier spectra, and the transfer function of the system under different illumination patterns. (c) Reconstruction flow chart of DPC-IDT.

DPC-IDT is constructed on a bright-field microscope (IX83, Olympus) with the illumination system replaced by a programmable annular LED source. The LED source consisting of 45 LED elements is placed 48.9 mm away from the sample stage, and each LED provides quasi-monochromatic plane wave illuminations with a center wavelength of 520 nm and an illumination NA of 0.75 that matches the NA of the objective lens (40×/0.75 UPLSAPO, Olympus). By controlling the on or off state of each LED through the ARM controller, any illumination mode can be obtained. Figure 1(a) presents the schematic of our experimental setup along with the illumination strategy. The captured intensity images, intensity spectra, and corresponding transfer function for different numbers of LEDs ($N = 1, 7, 24$) are depicted in Fig. 1(b). Note that the LEDs on each illumination pattern are switched on at the same time. It is found that asymmetric annular illumination enhances the POTF, providing a robust spectral response within the incoherent diffraction limit. This ensures that the entire phase information of the sample is transmitted into the intensity image in parallel. Based on this, achieving isotropic resolution for RI and absorption reconstruction requires recording at least four annular DPC images with a CMOS camera (Hamamatsu ORCA-Flash 4.0 C13440, pixel resolution, 2048 × 2048; pixel pitch, 6.5 μm) . With the camera exposure rate of 100 Hz, DPC-IDT can realize a 25 Hz imaging rate. Figure 1(c) presents the DPC-IDT implementation strategy for the raw images captured under four annular DPC illuminations. Each DPC illumination pattern controlled to turn on sequentially by the ARM board controller and pass through the sample, the camera is employed to record four focused intensity images sequentially in the image plane. The linear relationship between the intensity image and the permittivity contrast allows us to efficiently solve for the 3D RI and absorption distributions of the samples using a slice-wise deconvolution algorithm. The closed-form solutions for real and imaginary permittivity

contrast at each axial slice are as follows:

$$\Delta\varepsilon_{re}(\mathbf{x},z)=\mathcal{F}^{-1}\left\{\frac{1}{C}\left[\left(\sum_{m=1}^{M}\left|H_{A,m}^{pc}(\mathbf{u},z)\right|^{2}+\beta\right)\left(\sum_{m=1}^{M}H_{P,m}^{pc*}(\mathbf{u},z)\,\tilde{I}_{m}\right)-\left(\sum_{m=1}^{M}H_{P,m}^{pc*}(\mathbf{u},z)\,H_{A,m}^{pc}(\mathbf{u},z)\right)\left(\sum_{m=1}^{M}H_{A,m}^{pc*}(\mathbf{u},z)\,\tilde{I}_{m}\right)\right]\right\},\tag{4a}$$

$$\Delta\varepsilon_{im}(\mathbf{x},z)=\mathcal{F}^{-1}\left\{\frac{1}{C}\left[\left(\sum_{m=1}^{M}\left|H_{P,m}^{pc}(\mathbf{u},z)\right|^{2}+\alpha\right)\left(\sum_{m=1}^{M}H_{A,m}^{pc*}(\mathbf{u},z)\,\tilde{I}_{m}\right)-\left(\sum_{m=1}^{M}H_{A,m}^{pc*}(\mathbf{u},z)\,H_{P,m}^{pc}(\mathbf{u},z)\right)\left(\sum_{m=1}^{M}H_{P,m}^{pc*}(\mathbf{u},z)\,\tilde{I}_{m}\right)\right]\right\},\tag{4b}$$

where $\mathcal{F}^{-1}$ denotes the 2D inverse Fourier transform, C is a normalization term $\left(\sum_{m=1}^{M}\left|H_{P,m}^{pc}(\mathbf{u},z)\right|^{2}+\alpha\right)\left(\sum_{m=1}^{M}\left|H_{A,m}^{pc}(\mathbf{u},z)\right|^{2}+\beta\right)-\left(\sum_{m=1}^{M}H_{P,m}^{pc}(\mathbf{u},z)\,H_{A,m}^{pc*}(\mathbf{u},z)\right)\left(\sum_{m=1}^{M}H_{P,m}^{pc}(\mathbf{u},z)\,H_{A,m}^{pc*}(\mathbf{u},z)\right)$, and m indexes the m'th illumination pattern. α and β are the regularization parameters for the phase and absorption. In summary, the absorption and phase of a sample can be reconstructed using intensity images and partially coherent absorption and phase optical transfer functions by slice-wise deconvolution.

To validate the capability of DPC-IDT for quantitative 3D RI reconstruction, a multi-layer cluster of microspheres (Polysciences, calibrated $n=1.595$ at $\lambda=512$ nm) with different sizes immersed in matched oil (Cargille, $n_m=1.58$) were implemented for tomographic imaging. We use four DPC intensity images to reconstruct 41 RI slices with a 1.5 μm step from −30 μm to 30 μm. Figure 2(a) displays the raw intensity images acquired under annular DPC illumination. The x–y and y–z slices of the reconstructed RI results using DPC-IDT are shown in Fig. 2(b), demonstrating the feasibility of the proposed method for 3D RI reconstruction. Due to the inevitable missing-cone problem, the recovered microsphere exhibits an elongation along the z axis. Additionally, we compared the reconstructed RI tomograms using the 24-frame IDT, 4-frame IDT, and DPC-IDT [Fig. 2(c)]. We found that the imaging quality of DPC-IDT is comparable to that of the conventional 24-frame IDT for samples with simple structures and sparse distributions, such as microspheres, given the same spectral support domain. The 4-frame IDT shows very poor imaging results due to the inadequate acquisition of spectral information led by only four coherent illuminations. The line profiles across the microspheres are illustrated in Fig. 2(d) to further quantitatively prove the above conclusions. Figure 2(e) shows a 3D rendered visualization of the reconstruction volume using DPC-IDT, clearly capturing the spherical geometry of the microsphere cluster.

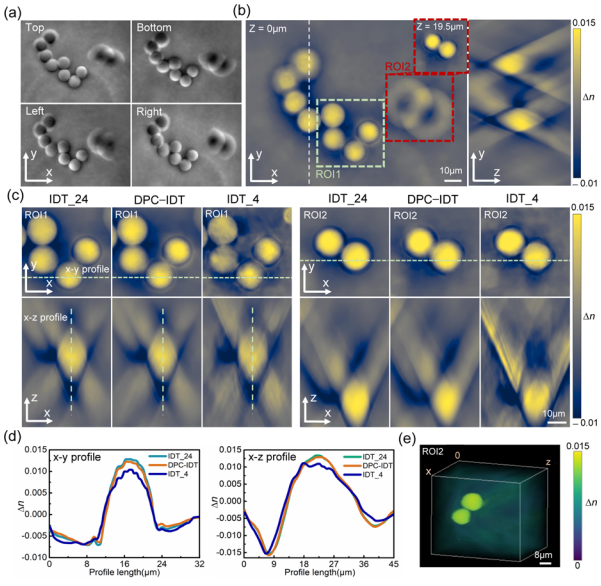

Fig. 2. Experiments on 3D RI tomography of polystyrene microspheres using different reconstruction strategies. (a) Raw intensity images acquired under annular DPC illumination. (b) Lateral and axial RI slices of the reconstructed microsphere clusters. (c) Comparison of the reconstructed RI tomograms using the 24-frame IDT, 4-frame IDT, and DPC-IDT. (d) Line profiles across the microsphere quantitatively represent the difference of RI results under three reconstruction strategies. (e) 3D rendering of the reconstructed microspheres results using DPC-IDT.

Next, we implemented tomographic imaging on unstained fixed HeLa cells to illustrate the biological applications of DPC-IDT. We have reconstructed 21 RI slices with a spacing of 0.8 μm between −8 μm and 8 μm. Figure 3(a) shows the reconstructed RI tomogram at 0 μm z plane, from which two representative regions of interest (ROI) are further enlarged in Fig. 3(b) for better demonstration of cell morphology details at different axial planes. The filopodia (circles), cellular membrane folds, and other high-RI organelles, including nucleoli, and lipid droplets (arrows) can be observed clearly. Moreover, the reconstructed results of ROI3 using the 24-frame IDT and DPC-IDT techniques are compared in Fig. 3(c). It can be found that the imaging quality of the two methods is almost the same near the in-focal plane. However, as the reconstructed RI tomograms move progressively away from the in-focal plane, the imaging quality of DPC-IDT will decrease slightly [circles in Fig. 3(c)]. This is because, although the spectral information obtained by the two methods is the same, the response of the partially coherent POTF

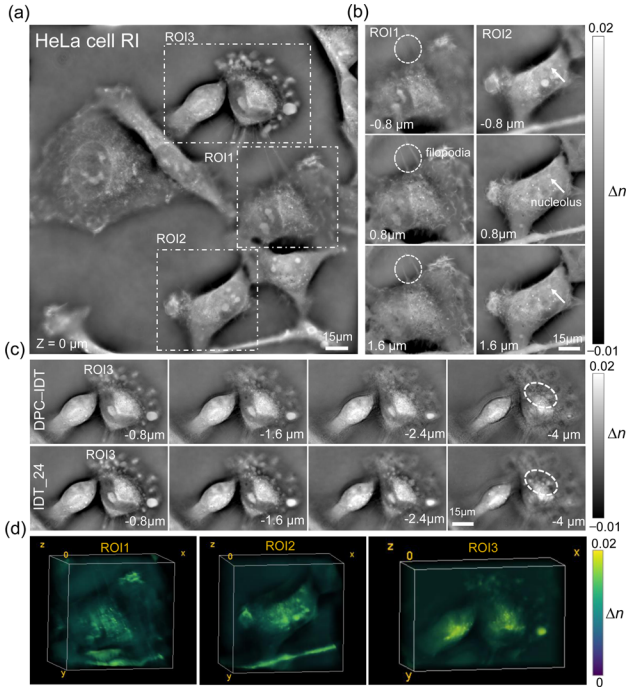

Fig. 3. Tomographic RI reconstruction of fixed HeLa cells. (a) Reconstructed RI tomogram of HeLa cells at 0 μm z plane. (b) RI tomograms at different depths for two ROIs. (c) Comparison of the 24-frame IDT and DPC-IDT for the RI reconstruction of the same subregion at different axial planes. (d) 3D rendering of HeLa cells.

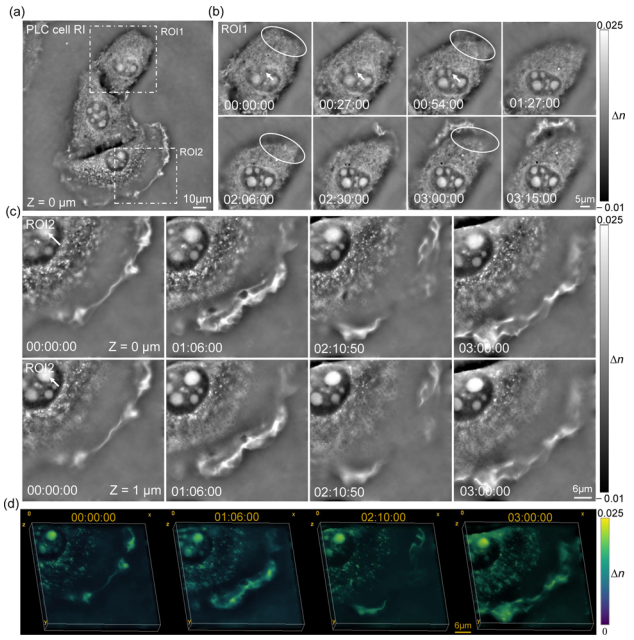

Fig. 4. Dynamic 3D RI imaging of living PLC cells over a long time. (a) Recovered RI tomogram of PLC cells located at 0 μm z plane at the start time point of 00:00:00. (b), (c) Enlarged time-lapse tomographic RI images of two different ROIs (see also Visualization 3). (d) 3D RI rendering of PLC cells at four different time points in ROI2.

on the defocused plane is weaker than that of the POTF in the coherent case, resulting in weaker phase contrast information of the sample far from the defocused plane. The comparison results for the RI reconstruction of HeLa cells at different axial planes are animated in Visualization 1. Figure 3(d) shows the 3D rendering of the reconstructed RI volumes, presenting the structural features of HeLa cells (see Visualization 2 for the corresponding 3D RI rendering of ROI2).

Although the imaging quality of DPC-IDT is slightly reduced compared with the traditional IDT technique, the significant advantage of our proposed method is that DPC-IDT can achieve high-speed 3D tomographic imaging with only four intensity images that need to be acquired in a short exposure time, achieving an imaging frame rate of 25 Hz. Figure 4 presents the dynamic 3D RI imaging of living PLC cells over a long time. The 21 RI slices were reconstructed in steps of 1 μm over the range of −10 μm–10 μm. A cropped region from the RI tomogram at 0 μm z plane, containing three whole PLC cells, is illustrated in Fig. 4(a). To better highlight subcellular details and dynamics at different moments, two ROIs are zoomed in, as shown in Figs. 4(b) and 4(c). The dynamic process of cell morphological changes [circles in Fig. 4(b)] and molding of nucleolus [arrows in Fig. 4(b)] can be clearly monitored (see also Visualization 3). Figure 4(b) further provides the dynamic 3D RI imaging results of another PLC cell at two different axial planes. Many small particles with high RI, possibly lipid droplets, lysosomes, or other organelles, are observed inside the cell, and the contour of the cell membrane edge can be clearly visible. As monitoring progresses, the cell membrane folds and curls with an obvious increase in its RI value (see also Visualization 3). At last, 3D volume-rendered views of reconstructed PLC cells at four different time points in ROI2 are displayed in Fig. 4(d) to visually represent the 3D structure changes over a long time (see Visualization 3 for the corresponding 3D RI rendering of ROI1 and ROI2).

In conclusion, we have proposed the DPC-IDT technique to realize high-speed 3D RI tomographic imaging with the volumetric imaging rate of 25 Hz. By seamlessly integrating traditional IDT with the DPC illumination scheme within the derived partially coherent IDT framework, DPC-IDT allows retrieving 3D RI tomograms from only four intensity images by employing a partially coherent slice-wise deconvolution algorithm. Compared to previous IDT methods, the proposed DPC-IDT improves at least twofold in terms of the number of images and imaging speed. Dynamic tomographic imaging of living PLC cells indicates the potential of DPC-IDT for the high-speed dynamic behavior of unstained samples.

Although the proposed DPC-IDT has the above advantages, it essentially incorporates information multiplexing and demultiplexing in the inverse scattering problem solution [19,20] compared to the traditional IDT technique. It is therefore reasonable to doubt whether this deconvolution algorithm is capable of achieving completely correct information demultiplexing. Particularly at the defocused plane, the partially coherent POTF exhibits a weak response and begins to decay with increasing defocus distance. This poses severe challenge to the retrieval of RI tomograms far from the in-focus plane and limits the reconstructed depth of the field. Fortunately, our proposed method is mainly aimed at studying the high-speed biological behavior of living cell samples, which are 3D thin samples (about 20 μm), and thus DPC-IDT performs well. Improving the measurement accuracy and expanding the reconstruction depth within our framework will be the main focus of future research.

Funding. National Natural Science Foundation of China (U21B2033, 62227818); National Key Research and Development Program of China (2022YFA1205002); Fundamental Scientiffc Research Business Fee Funds for the Central Universities (2023102001); Jiangsu Key Laboratory of Spectral Imaging and Intelligence Sense (JSGP202201).

Disclosures. The authors declare no conflicts of interest.

Data availability. Data underlying the results presented in this Letter are not publicly available but may be obtained from the authors upon reasonable request.

REFERENCES

1. E. Wolf, Opt. Commun. **1**, 153 (1969).
2. W. Choi, C. Fang-Yen, K. Badizadegan, *et al.*, Nat. Methods **4**, 717 (2007).
3. Y. Sung, W. Choi, C. Fang-Yen, *et al.*, Opt. Express **17**, 266 (2009).
4. Y. Cotte, F. Toy, P. Jourdain, *et al.*, Nat. Photonics **7**, 113 (2013).
5. R. Horstmeyer, J. Chung, X. Ou, *et al.*, Optica **3**, 827 (2016).
6. C. Zuo, J. Sun, J. Li, *et al.*, Opt. Lasers Eng. **128**, 106003 (2020).
7. S. Zhou, J. Li, J. Sun, *et al.*, Optica **9**, 1362 (2022).
8. J. M. Soto, J. A. Rodrigo, and T. Alieva, Opt. Express **25**, 15699 (2017).
9. R. Ling, W. Tahir, H.-Y. Lin, *et al.*, Biomed. Opt. Express **9**, 2130 (2018).
10. A. Matlock and L. Tian, Biomed. Opt. Express **10**, 6432 (2019).
11. J. Li, A. Matlock, Y. Li, *et al.*, Adv. Photonics **1**, 066004 (2019).
12. J. M. Soto, J. A. Rodrigo, and T. Alieva, Appl. Opt. **57**, A205 (2018).
13. J. M. Soto, J. A. Rodrigo, and T. Alieva, Opt. Lett. **43**, 4699 (2018).
14. J. Huang, Y. Bao, and T. K. Gaylord, J. Opt. Soc. Am. A **37**, 1857 (2020).
15. H. Hugonnet, M. Lee, and Y. Park, Opt. Express **29**, 6293 (2021).
16. L. Tian and L. Waller, Opt. Express **23**, 11394 (2015).
17. H. Lu, J. Chung, X. Ou, *et al.*, Opt. Express **24**, 25345 (2016).
18. Y. Fan, J. Sun, Q. Chen, *et al.*, Photonics Res. **7**, 890 (2019).
19. J. Sun, Q. Chen, J. Zhang, *et al.*, Opt. Lett. **43**, 3365 (2018).
20. L. Tian and L. Waller, Optica **2**, 104 (2015).